

Hydrophobic effects in interfacial environments

Amish J. Patel,¹ Patrick Varilly,² Sumanth N. Jamadagni,¹

Hari Acharya,¹ Shekhar Garde,^{1,*} and David Chandler^{2,*}

¹*Howard P. Isermann Department of Chemical & Biological Engineering,
and Center for Biotechnology and Interdisciplinary Studies,
Rensselaer Polytechnic Institute, Troy, NY 12180, USA*

²*Department of Chemistry, University of California, Berkeley, CA 94720, USA*

Abstract

We study the solvation thermodynamics of hydrophobic solutes in water near self-assembled monolayers (SAMs) using atomistic numerical simulation and theory. We consider SAMs with a range of chemistries, from hydrophilic to hydrophobic, and solutes with a range of sizes from sub-nanometer to a few nanometers. We show that the temperature variation of solvation free energy depends non-trivially on surface hydrophobicity and solute size. This temperature variation is explained in terms of the interplay between interfacial fluctuations and excluded volume effects—the physical effects encoded in Lum-Chandler-Weeks theory [J. Phys. Chem. B 103:4570–4577 (1999)]. Our results also show that hydrophobic forces of assembly in the vicinity of an extended hydrophobic surface are weaker than those in bulk aqueous solution, from which we suggest a catalytic role for extended hydrophobic interfaces in unfolding of proteins, as occurs in amyloids and the interior of chaperonins. We further show that this driving force for assembly decreases with increasing temperature near hydrophobic surfaces, in contrast to that in bulk water.

Keywords: hydrophobicity, interfaces, thermodynamics, assembly, binding

* To whom correspondence should be addressed. Email: gardes@rpi.edu or chandler@berkeley.edu

The physics of hydrophobic hydration in bulk water depends on solute lengthscale [1–3], changing gradually from being entropic at small lengthscales ($\lesssim 1$ nm) [4–7] to being enthalpic at larger lengthscales [8–10]. An interplay between the two regimes can be important, for instance, when small species self-assemble into a large aggregate in bulk water. Interfacial environments present a different context for solvation and assembly. To explore hydrophobic effects at interfaces, we study the solvation of solutes of different sizes near interfaces of varying hydrophobicity. The techniques we use are molecular simulation and theory. We show that at hydrophobic surfaces, solvation at all lengthscales (including small ones) is enthalpic. As a result, the driving force for assembly at hydrophobic interfaces decreases with temperature, whereas in bulk, it increases with temperature. Our findings also suggest that the driving force for assembly is smaller at hydrophobic interfaces than it is in bulk.

A. Models

Fig. 1(a) shows the setup that we use in molecular dynamics (MD) simulations for studying hydration at interfaces. We focus on the solid-water interfaces of self-assembled monolayers (SAMs) of surfactants presenting a range of head-group chemistries, from hydrophobic ($-\text{CH}_3$) to hydrophilic ($-\text{OH}$). This system is similar to that used previously to study interfacial hydration [11] and thermal transport [12]. Simulations were performed in the NVT ensemble with a periodic box ($7 \text{ nm} \times 7 \text{ nm} \times 9 \text{ nm}$) that has a buffering liquid-vapor interface at the top of the box, for reasons explained in ref. [13]. It has been shown that free energies obtained in the above ensemble are indistinguishable from those obtained in the NPT ensemble at a pressure of 1 bar [14]. The water model used is SPC/E [15]. We characterize the temperature-dependent hydration of cuboid-shaped cavities ($L \times L \times W$, $W = 0.3 \text{ nm}$) of various sizes (L) in bulk water and at SAM-water interfaces. We select cavity volumes of cuboid shape and 0.3 nm thickness because they are particularly sensitive to phenomena at interfaces. Thicker volumes will show qualitatively similar behavior, but will gradually sample the “bulk” region away from the interface. To study lengthscale-dependent hydration, we vary L from small values comparable to the size of a water molecule to as large as ten times that size. Solvation free energies are calculated using test particle insertions [16] for smaller cavities ($L < 1 \text{ nm}$), and indirect umbrella sampling (INDUS) [13, 14] for larger

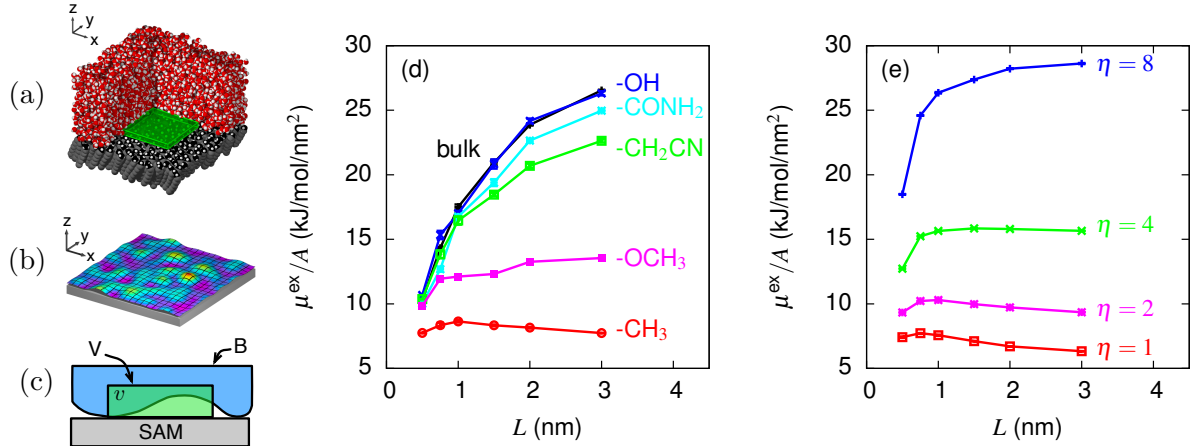


FIG. 1. (a) A schematic of part of the system, with an $L \times L \times W$ cuboidal cavity (green) at the SAM-water interface. The surfactant head groups (black and white), their alkane tails (grey), and water (red and white, partially cut away for clarity) are shown. (b) A typical configuration of the model interface $z = h(x, y)$ (color-coded by z). The grey region represents the model surface. (c) Important volumes in estimating the free energy μ^{ex} of emptying the probe volume V (green) via Eq. (2). The region $z > h(x, y)$ is the volume B (blue), and the intersection of V and B is v (dark green) (d) Lengthscale dependence of the cavity solvation free energy per unit area, μ^{ex}/A , in bulk water and at interfaces, at $T = 300$ K, measured using MD simulations. (e) μ^{ex}/A , estimated using Eq. (2), near surfaces with different attraction strengths η .

cavities.

To rationalize the behavior found from atomistic simulations, we have also developed an independent model that implements the ideas of Lum-Chandler-Weeks (LCW) theory [1]. This theory predicts the existence of a soft liquid-vapor-like interface near hydrophobic surfaces, consistent with Stillinger’s proposal [8]. By a “soft interface”, we mean that substantial deformations of the interface cost relatively little free energy. Since it is soft, dispersive interactions are strong enough to pull the interface right up against the surface, so that the mean water density next to the surface does not reflect its hydrophobicity [11]. The signature of the soft interface, as confirmed by recent simulations [13], is instead, the relative ease with which a cavity can be created near a hydrophobic surface, compared to that in bulk.

Here, we model the liquid-vapor-like interface as a periodic elastic membrane, $z = h(x, y)$, with an associated Hamiltonian, $H[h(x, y)]$, that captures its surface tension and its inter-

action with the underlying surface,

$$H[h(x, y)] = \int_{x, y} \left[\frac{\gamma}{2} |\nabla h(x, y)|^2 + \int_{z=h(x, y)}^{\infty} \rho_{\ell} U(\mathbf{r}) \right]. \quad (1)$$

Here, γ is the experimental liquid-vapor surface tension of water, ρ_{ℓ} is the bulk number density of water, and $U(\mathbf{r})$ is the interaction potential between the model surface and a water molecule at position $\mathbf{r} = (x, y, z)$. The square-gradient term in Eq. (1) accurately captures the energetics of interfacial capillary waves only for wavelengths that are large compared to atomic dimensions, so we restrict $h(x, y)$ to contain only modes with wavevectors below $2\pi/9 \text{ \AA}$ (see Appendix). Fig 1(b) depicts a typical configuration of $h(x, y)$.

Fig 1(c) shows a side view of an $L \times L \times W$ probe volume, V , located at the surface-water interface. At any instant in time, part of V can be empty due to an interfacial fluctuation. The number of waters in the remaining volume, v , fluctuates, and we denote by $P_v(N)$ the probability that v contains N waters. We thus estimate the free energy for emptying V completely to be

$$\mu^{\text{ex}}(V) = -k_{\text{B}}T \ln \int \mathcal{D}h Z^{-1} e^{-\beta H[h(x, y)]} P_v(0), \quad (2)$$

where $Z = \int \mathcal{D}h \exp\{-\beta H[h(x, y)]\}$ is the partition function of the membrane. The volume v depends on the interfacial configuration $h(x, y)$, *i.e.*, $v = v[h(x, y)]$.

It is known that $P_v(N)$ is well-approximated by a Gaussian when v is small [4, 11, 17]. If water were far from liquid-vapor coexistence, then $P_v(N)$ would also be close to Gaussian for arbitrarily large v . The fact that water at ambient conditions is near liquid-vapor coexistence, and that there is a liquid-vapor-like interface near the SAM, is captured by the additional interfacial energy factor $Z^{-1} \exp\{-\beta H[h(x, y)]\}$ in Eq. (2). The net result is that the thermal average of Eq. (2) is dominated by interface configurations where v is small, so that even at ambient conditions, we can approximate

$$P_v(N) \approx (2\pi\sigma_v)^{-1/2} \exp \left[-(N - \langle N \rangle_v)^2 / 2\sigma_v \right],$$

where $\langle N \rangle_v$ is the average number of waters in v and $\sigma_v = \langle (\delta N)^2 \rangle_v$ is the variance. We estimate these by noting that the solvent density responds linearly to the attractive potential, $U(\mathbf{r})$, in the volume occupied by the water, B , depicted in Fig. 1(c) [4, 5, 18]. Hence,

$$\begin{aligned} \langle N \rangle_v &\approx \rho_{\ell} v - \int_{\mathbf{r} \in v} \int_{\mathbf{r}' \in B} \chi(\mathbf{r}, \mathbf{r}') \beta U(\mathbf{r}'), \\ \sigma_v &\approx \int_{\mathbf{r} \in v} \int_{\mathbf{r}' \in v} \chi(\mathbf{r}, \mathbf{r}'), \end{aligned}$$

where

$$\chi(\mathbf{r}, \mathbf{r}') = \rho_\ell \delta(\mathbf{r} - \mathbf{r}') + \rho_\ell^2 [g(|\mathbf{r} - \mathbf{r}'|) - 1].$$

Here, $g(r)$ is the oxygen-oxygen radial distribution function of water [19].

The surface–water interaction is modeled by a potential, $U(\mathbf{r})$, chosen to closely mimic the attractive potential that the $-\text{CH}_3$ SAM exerts on the water above it. It is composed of three terms,

$$U(\mathbf{r}) = U_{\text{wall}}(\mathbf{r}) + \eta U_{\text{head}}(\mathbf{r}) + U_{\text{tail}}(\mathbf{r}).$$

The first term, $U_{\text{wall}}(\mathbf{r})$, is a sharply repulsive potential in the region $z < R_0$ that captures the hard-core exclusion of a plane of head groups at $z = 0$ with hard-sphere radius R_0 . The second term, $U_{\text{head}}(\mathbf{r})$, captures the head group–water interaction, with the head groups modeled as a plane of Lennard-Jones (LJ) interaction sites of area density μ_{head} at $z = 0$ and the LJ parameters of an OPLS/UA CH_3 group interacting with an SPC/E water oxygen atom [20]. It is scaled by a parameter η that we discuss shortly. The final term, $U_{\text{tail}}(\mathbf{r})$, similarly captures the alkane tail–water interaction, with the tail groups modeled as a uniform half-space of LJ interaction sites of volume density ρ_{tail} at a distance ζ below the head groups and the LJ parameters of an OPLS/UA CH_2 group interacting with an SPC/E water oxygen atom. The parameters R_0 , ζ , μ_{head} and ρ_{tail} are dictated by the geometry of the SAM. Their values and the explicit form of the potential are given in the Supplementary Information.

The parameter η is used to tune the strength of the surface–water interaction. A value of 1 corresponds to a $-\text{CH}_3$ -SAM-like surface, and higher values result in surfaces that are more hydrophilic. Such surfaces, however, lack the specific details of hydrogen bonding interactions (*e.g.*, between an $-\text{OH}$ SAM surface and water) so comparisons between high- η model surfaces and hydrophilic SAM surfaces in simulations are qualitative in nature.

B. Size dependent hydrophobic hydration at interfaces

Fig. 1(d) shows the excess free energy, μ^{ex} , to solvate a cavity at temperature $T = 300$ K, divided by the it’s surface area ($A = 2L^2 + 4LW$). μ^{ex}/A can be thought of as an effective surface tension of the cavity-water interface. When the cavity is situated in bulk water, this value shows a gradual crossover with increasing L . For the largest L studied here (3 nm), $\mu^{\text{ex}}/A \approx 26$ kJ/mol/nm², which is less than the surface tension of SPC/E water (about 38

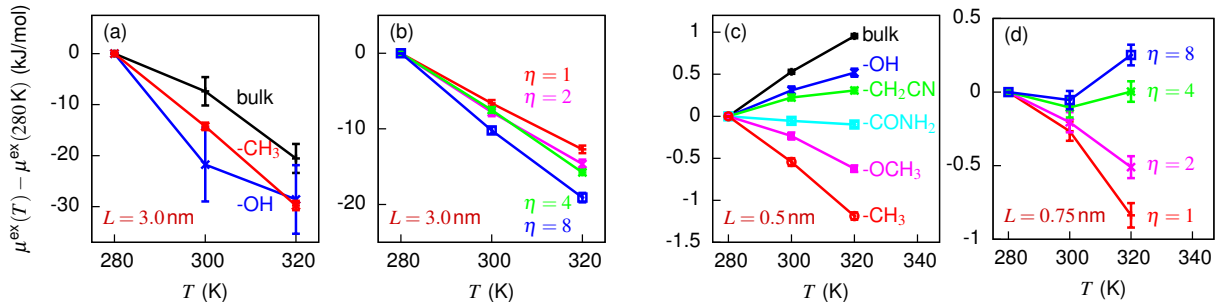


FIG. 2. Temperature dependence of μ^{ex} in bulk water and at SAM-water interfaces for (a-b) large ($L = 3.0$ nm) and (c-d) small ($L = 0.5$ nm, $L = 0.75$ nm) cavities, obtained from simulations (a,c) and from the model (b,d) of Eq. (2).

kJ/mol/nm² [21]). Such a difference is expected for two reasons. First, as with spherical solutes, the high curvature of small solutes induces curvature corrections to the surface tension [22]. Second, since W is small (0.3 nm) even when L is large, the interactions of water molecules across the cavity width lower the effective surface tension.

The lengthscale dependence of μ^{ex}/A for solvating cavities in interfacial environments, shown in Fig. 1(d) is particularly interesting. Near the hydrophilic OH-terminated SAM, the behavior is similar to that in bulk water. However, with increasing hydrophobicity of the interface, the size dependence of μ^{ex}/A becomes less pronounced and is essentially absent near the -CH₃ surface. For $L \gtrsim 1.5$ nm, it is possible to correlate the macroscopic hydrophobicity of each SAM surface, to the difference between μ^{ex} at the surface and in bulk, as shown in the Appendix.

Fig. 1(e) shows the analogous solvation free energies calculated using Eq. (2). The essential features of solvation next to the SAM surfaces are captured well by this model. This is particularly true for the hydrophobic surfaces (with η around 1), where the potential $U(\mathbf{r})$ closely mimics the effect of the real SAM on the adjacent water, and the agreement between theory and simulation is nearly quantitative. For the more hydrophilic SAMs, as stated above, the comparison is qualitative, because the simple form for $U(\mathbf{r})$ does not represent dipolar interactions well.

C. Temperature dependence of hydration at interfaces

The temperature dependence of μ^{ex} characterizes the entropic and enthalpic contributions to the free energy, and clearly highlights the differences between hydration at interfaces and in bulk. For small solutes in bulk, the entropy of hydration is known to be large and negative, which reflects the reduced configurational space available to the surrounding water molecules [7, 9]. In contrast, for large solutes the entropy of hydration is expected to be positive, consistent with the temperature dependence of the liquid-vapor surface tension (about 90 J/mol/K/nm² [23]). Fig. 2(a) shows that μ^{ex} of large cuboidal cavities ($L = 3$ nm) in bulk water indeed decreases with temperature giving entropy per unit surface area to be about 25 J/mol/K/nm². Solvation entropies in SPC/E water obtained using NPT ensemble MD simulations are known to be smaller than experimental values by about 20% [24]. Some differences are also expected based on the arguments given above for differences in cavity and liquid-vapor interfacial tensions.

Fig. 2(a) also shows that for large cuboidal cavities ($L = 3$ nm), μ^{ex} decreases with increasing temperature not only in bulk water and near the hydrophilic (-OH) surface, but also near the hydrophobic (-CH₃) surface, indicating a positive entropy of cavity formation. Thus, in all three systems, the thermodynamics of hydration of large cavities is governed by interfacial physics. Although the values of $\mu^{\text{ex}}(L = 3$ nm) at 300 K are rather large (569 kJ/mol in bulk water, 565 kJ/mol at the -OH interface, and 167 kJ/mol at the -CH₃ interface), their variation with temperature shown in Fig. 2(a) is similar in bulk and at interfaces.

Fig. 2(b) shows that this same phenomenology is captured nearly quantitatively by the simple model of Eq. (2). In the model, the solvation free energies of these probe volumes have large but athermal contributions from the attractions between water and the model surface. The main temperature-dependent contribution to μ^{ex} is the cost to deform the liquid-vapor-like interface near the surface to accommodate the large probe volume. Since the necessary deformation is similar, regardless of the hydrophobicity of the surface, the variation of μ^{ex} with temperature is similar as well.

Fig. 2(c) shows the temperature dependence of μ^{ex} for small cavities ($L = 0.5$ nm) in bulk and at SAM-water surfaces. The volume of this cavity is somewhat smaller than that required to insert an argon atom. In bulk water, μ^{ex} increases with temperature, and

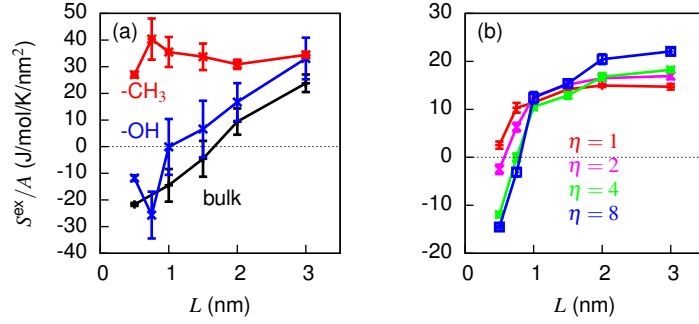


FIG. 3. Lengthscale dependence of the excess solvation entropy per unit surface area for (a) cavities in bulk water and at the -CH₃ and -OH SAM-water interfaces, and (b) cavities in the model of Eq. (2) near surfaces of different attraction strengths, η .

yields an entropy of hydration of roughly -25 J/mol/K, characteristic of small lengthscale hydrophobic hydration. This negative value is consistent with those calculated for spherical solutes of a similar volume [7]. With increasing hydrophobicity, the slope of the μ^{ex} vs T curve decreases and becomes negative, indicating a positive entropy of cavity formation near sufficiently hydrophobic surfaces. Near the most hydrophobic surface (-CH₃), the entropy of hydration of this small cavity is $+30$ J/mol/K.

Fig. 2(d) shows that the same phenomenon is recovered by the simple model of Eq. (2), though the correspondence is clearest at a slightly larger cavity size ($L = 0.75$ nm). Near hydrophilic model surfaces, the interface is pulled close to the surface by a strong attraction, so it is costly to deform it. As a result, the cavity is emptied through bulk-like spontaneous density fluctuations that result in a negative entropy of hydration of small cavities. In contrast, near a hydrophobic surface, the interface is easy to deform, which provides an additional mechanism for creating cavities. In fact, this mechanism dominates near sufficiently hydrophobic surfaces, and since the surface tension of water decreases with increasing temperature, so does μ^{ex} . Hence, even small cavities have a positive entropy of hydration near hydrophobic surfaces. The continuous spectrum of negative to positive solvation entropies observed in Figs. 2(c-d) is thus revealed to be a direct consequence of the balance between bulk-like water density fluctuations and liquid-vapor-like interfacial fluctuations, represented explicitly by the two factors in the integrand of Eq. (2).

Fig. 3(a) shows that near the hydrophobic CH₃-terminated SAM, cavity hydration en-

tries per unit area, S^{ex}/A , are positive and essentially constant (about 30 J/mol/K/nm^2) over a broad range of cavity sizes. In contrast, in bulk water, S^{ex}/A depends on L , and changes from large negative to positive values with increasing L . The lengthscale at which entropy crosses zero, L_S , can serve as a thermodynamic crossover length. In bulk water, $L_S \approx 1.8 \pm 0.2 \text{ nm}$. The behavior of S^{ex}/A is qualitatively similar at the -OH surface, with $L_S \approx 1.3 \pm 0.4 \text{ nm}$. Although the numerical value of L_S may depend on the shape of the cavity and on solute-water attractions for non-idealized hydrophobes, the trend in entropy should not.

Fig. 3(b) shows that our simple implementation of LCW ideas recovers many of the observed trends, with solvation entropy being everywhere positive for the smallest attraction strength η , and a thermodynamic crossover length of just under 1 nm emerging for the more hydrophilic model surfaces, similar to that in bulk water. Nevertheless, the agreement between Figs. 3(a) and (b) is somewhat qualitative, mostly as a result of the crude form of $U(\mathbf{r})$ used to model hydrophilic surfaces.

D. Thermodynamics of binding to, and assembly at hydrophobic surfaces

In the preceding sections, we have examined the hydration behavior of a single isolated, idealized cavity near a flat surface and in the bulk. We now consider the consequences of our observations on hydrophobically driven binding and assembly, summarized schematically in Fig. 4.

Fig. 4 indicates that while the binding of both small and large solutes (or aggregates) to hydrophobic surfaces is highly favorable, their thermodynamic signatures are different. Binding of small solutes is entropic and becomes more favorable with increasing temperature, whereas binding of large solutes is enthalpic and depends only weakly on temperature.

Fig. 4 also highlights the differences in the thermodynamics of hydrophobically driven assembly at interfaces and in bulk, inferred from our lengthscale dependent studies. In bulk, the solvation of many small, isolated hydrophobes scales as their excluded volume. Accommodating small species inside the existing hydrogen-bonding network of water imposes an entropic cost, so the solvation free energy increases with increasing temperature. When several small hydrophobes come together, water instead hydrates the aggregate by surrounding it with a liquid-vapor-like interface. The corresponding solvation free energy scales as the

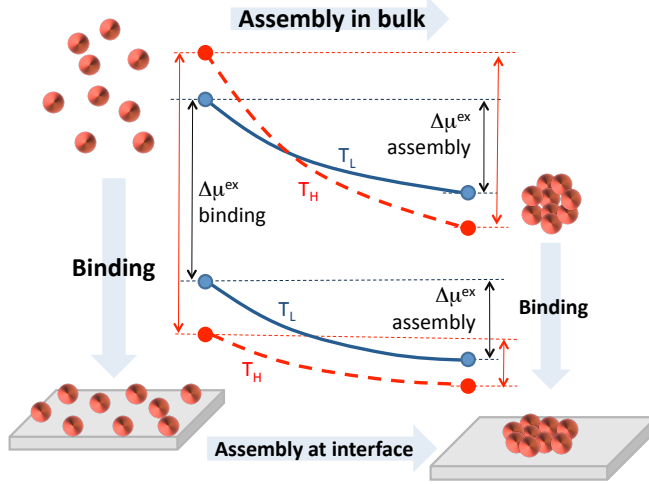


FIG. 4. Schematic illustrating the thermodynamics of binding and assembly. The points represent free energies of solvating small objects individually (left) and in the assembled state (right), in bulk (top) and at a hydrophobic interface (bottom), at a lower (blue, T_L) and a higher (red, T_H) temperature near ambient conditions. Assembly: The driving force for assembly at hydrophobic interfaces is smaller than that in bulk. It is enthalpic and decreases with increasing temperature, unlike in bulk. Binding: The driving force for binding small objects to a hydrophobic surface increases with temperature, so it is entropic. For large objects, it is enthalpic.

surface area and decreases with increasing temperature.

Thus, the driving force for assembly of n small solutes (each of surface area A_1 , volume v_1 and solvation free energy of $\mu_{1,\text{bulk}}^{\text{ex}}$) into a large aggregate (with surface area A_n and volume nv_1) in bulk water is well-approximated by

$$\Delta\mu_{\text{bulk}}^{\text{ex}} = \gamma_{\text{bulk}}A_n - n\mu_{1,\text{bulk}}^{\text{ex}} = [Cn^{-1/3} - 1]n\mu_{1,\text{bulk}}^{\text{ex}}, \quad (3)$$

where $C \sim (\gamma_{\text{bulk}}v_1^{2/3}/\mu_{1,\text{bulk}}^{\text{ex}})$ and γ_{bulk} is a curvature-corrected effective surface tension (top curve of Fig. 1(d)). For nanometer-sized aggregates hydrated at ambient conditions, $\Delta\mu_{\text{bulk}}^{\text{ex}}$ is large and negative (favorable), but decreases in magnitude and can even change sign with decreasing temperature (upper portion of Fig. 4). When adapted to particular systems, Eq. (3) can, with remarkable accuracy, explain complex solvation phenomena like the temperature-dependent aggregation behavior of micelles [25] and the cold denaturation of proteins [26].

In the presence of a hydrophobic surface, on the other hand, we have found that interfacial

physics dominates at all lengthscales (Fig. 2(a-d) and Fig. 3(a-b)). As a result, the driving force for assembly at interfaces, $\Delta\mu_{\text{int}}^{\text{ex}}$, does not scale as in Eq. (3), but is instead given by

$$\Delta\mu_{\text{int}}^{\text{ex}} = \gamma_{\text{int}}(A_n - nA_1) \sim [n^{-1/2} - 1]n\mu_{1,\text{int}}^{\text{ex}}, \quad (4)$$

where γ_{int} is the effective surface tension at the interface, (the lower curves of Figs. 1(d-e)). Since γ_{int} decreases with increasing temperature (Figs. 2(a-d)), the hydration contribution to the driving force for assembly weakens with increasing temperature at a hydrophobic surface, in contrast to that in bulk.

The free energy barrier between disperse and assembled states is also very different in bulk and near hydrophobic interfaces. In bulk, the dispersed state has no liquid-vapor-like interface whereas the assembled state does. The transition state consists of a critical nucleus of hydrophobic particles that nucleates the vapor-liquid-like interface. The nucleation barrier can be high, and dominates the kinetics of hydrophobic collapse of idealized hydrophobic polymers [27, 28] and plates [29]. In contrast, we expect aggregation near interfaces to be nearly barrierless, since an existing liquid-vapor-like interface is deformed continuously between the disperse and assembled states.

Finally, and most importantly, we find that for large aggregates, the driving force of assembly is weaker near interfaces than in bulk. In this limit, the terms $n\mu_1^{\text{ex}}$ dominate both at interfaces and in bulk (Eqns. (3) and (4)), and the results in Fig. 1(d) show that $\mu_{1,\text{int}}^{\text{ex}} < \mu_{1,\text{bulk}}^{\text{ex}}$.

The non-trivial behavior of the driving forces and barriers to assembly at interfaces should be relevant in biological systems where hydrophobicity plays an important role. Experiments have shown that hydrophobic surfaces bind and facilitate the unfolding of proteins, including those that form amyloids [30–32]. Our results shed light on these phenomena and suggest that large hydrophobic surfaces may generically serve as catalysts for unfolding proteins, via solvent-mediated interactions. Indeed, simulations show that the binding of model hydrophobic polymers to hydrophobic surfaces is accompanied by a conformational rearrangement from globular to pancake-like structures [33]. Such conformations can further assemble into tertiary structures, such as β -sheets [31, 32], and we predict that the solvent contribution to this assembly at the hydrophobic surface will be enthalpic in nature. This implies that reducing the liquid-vapor surface tension, either by increasing the temperature or by adding co-solutes, will reduce the hydration contribution to the driving force for

assembly.

We further speculate that the catalysis of unfolding by hydrophobic surfaces may play a role in chaperonin function [34]. The interior walls of chaperonins in the open conformation are hydrophobic and can bind misfolded proteins, whereupon their unfolding is catalyzed [35, 36]. Subsequent ATP-driven conformational changes render the chaperonin walls hydrophilic [34, 35]. As a result, the unfolded protein is released from the wall, as the free energy for a hydrophobe to bind to a hydrophilic surface is much lower than that to bind to a hydrophobic one (Fig. 1(d)).

Collectively, our findings highlight that assembly near hydrophobic surfaces is quite different from assembly in bulk and near hydrophilic surfaces. Experimental measurements on the thermodynamics of protein folding have been performed primarily in bulk water [37]. Although many experiments have probed how interfaces affect protein folding, structure and function [30, 38], to the best of our knowledge, there are no temperature-dependent thermodynamic measurements of self-assembly at interfaces. We hope that our results will motivate such measurements.

ACKNOWLEDGMENTS

AJP and PV were supported by NIH Grant No. R01-GM078102-04. SG gratefully acknowledges financial support of the NSF-NSEC (DMR-0642573) grant. DC was supported by the Director, Office of Science, Office of Basic Energy Sciences, Materials Sciences and Engineering Division and Chemical Sciences, Geosciences, and Biosciences Division of the U.S. Department of Energy under Contract No. DE-AC02-05CH11231.

APPENDIX

1. Microscopic characterization of hydrophobicity

For a ligand of a given size, the difference in the hydration free energies at an interface and in the bulk, $\Delta\mu^{\text{ex}} = \mu_{\text{int}}^{\text{ex}} - \mu_{\text{bulk}}^{\text{ex}}$, quantifies the hydration contribution to the experimentally measurable free energy of binding. As shown in Fig. 5, that free energy is small for binding to hydrophilic surfaces and increases in magnitude with increasing surface hydrophobicity, becoming highly favorable (i.e., negative) for hydrophobic surfaces.

Because the solvation of large solutes in bulk, and at hydrophobic and hydrophilic surfaces, is governed by the physics of interface formation, we can approximate

$$\Delta\mu^{\text{ex}} = A_c(\gamma_{\text{SV}} - \gamma_{\text{SL}} - \gamma_{\text{LV}}), \quad (5)$$

where $A_c = L^2$ is the cross-sectional area, γ is the surface tension, and subscripts SV, SL, and LV, indicate solid-vapor, solid-liquid, and liquid-vapor interfaces, respectively. Eq. (5) describes the fact that the original liquid-vapor interface (of the cavity in bulk water) and solid-liquid interface (where the solid interface is hydrated by water) are replaced by the solid-vapor interface in the associated state. Using Young's equation, $\gamma_{\text{SV}} = \gamma_{\text{SL}} + \gamma_{\text{LV}} \cos \theta$, we rewrite Eq. (5) as

$$\Delta\mu^{\text{ex}} = -A_c\gamma_{\text{LV}}(1 - \cos \theta), \quad (6)$$

where θ is the water droplet contact angle on the solid surface.

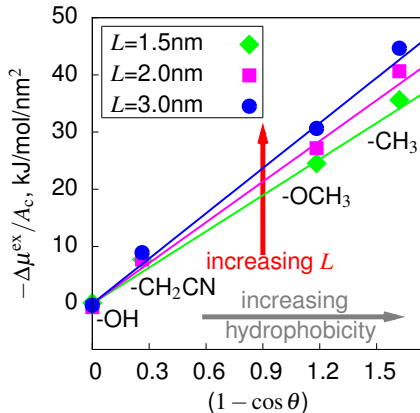


FIG. 5. Connecting the microscopic binding free energy of a cavity to a SAM-water interface, to the macroscopic wetting property of that interface. The values of $\cos \theta$ were obtained from MD simulations of a water droplet on SAM surfaces (reported in [12]). Lines are predictions using Eq. (6) with size dependent γ_{LV} taken from Fig. 1(d).

Although Eq. (6) is strictly valid only for macroscopic cavities, it can be applied to sufficiently large microscopic cavities with a lengthscale-dependent surface tension, $\tilde{\gamma}_{\text{LV}}$, which can be estimated by the quantity $\mu_{\text{bulk}}^{\text{ex}}/A$, shown in Fig. 1(d). Indeed, lines in Fig. 5 predicted using Eq. (6), with γ_{LV} substituted by $\tilde{\gamma}_{\text{LV}} \approx \mu_{\text{bulk}}^{\text{ex}}/A$, are in excellent agreement with simulation data. For a cavity of a given size, the strength of its binding increases with

surface hydrophobicity, as expected. Also, $\tilde{\gamma}_{LV}$ increases with L , indicating that binding is inherently stronger for larger cavities.

Collectively, the data in Fig. 5 establish a connection between the binding of large yet microscopic hydrophobic solutes ($L > 1$ nm) to different SAM interfaces, and the macroscopic wetting properties of those interfaces, as characterized by their contact angles. This connection provides a molecular-level framework to characterize the hydrophobicity of complex interfaces, such as those of proteins and biomolecules. These interfaces are chemically and topographically heterogeneous at the nanoscale, which has been shown to affect surface hydrophobicity [39–41]. Despite this complexity, μ^{ex} at these interfaces includes information about how water responds to the local context, and allows characterization of interfacial hydrophobicity.

2. Power spectrum of a free vapor-liquid interface

We simulate a liquid-vapor interface in a large slab of SPC/E water at 300 K, and evaluate the instantaneous interface configuration, $h(x, y)$, and its Fourier transform, $\tilde{h}(\mathbf{k})$, using a definition that is appropriate for atomistic systems [42]. Capillary-wave theory predicts that the power spectrum of interfacial fluctuations, $\langle |\tilde{h}(\mathbf{k})|^2 \rangle$, scales as $1/\beta\gamma k^2$. As shown in Fig. 6, we find good agreement between the power spectrum of our simulated instantaneous interface and capillary-wave theory prediction for wavevectors smaller than about $2\pi/9$ Å. For larger wavevectors, the power spectrum is sensitive to molecular detail, as expected [43].

SUPPLEMENTARY INFORMATION

Here, we describe the details of the solvation model used in the main text.

Interface description

We describe the liquid-vapor-like interface next to the model surface by a periodic height function $h(\mathbf{a})$, with $\mathbf{a} = (x, y)$ and $-D/2 \leq x, y < D/2$. This function is sampled discretely at a resolution Δ , at points satisfying

$$\mathbf{a} = (n_x\Delta, n_y\Delta), \quad -\frac{D}{2\Delta} \leq n_x, n_y < \frac{D}{2\Delta}.$$

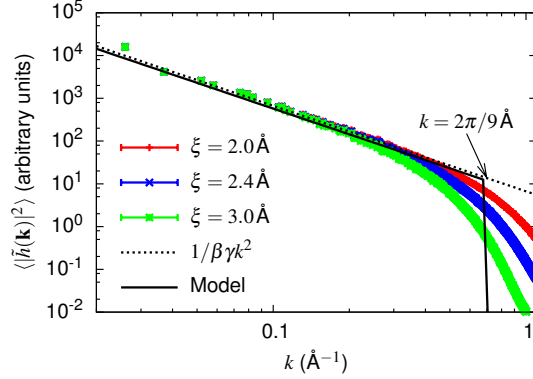


FIG. 6. Power spectrum of the intrinsic interface of Ref. [42] for SPC/E water at a temperature of 300 K, measured in a $24 \times 24 \times 3 \text{ nm}^3$ slab of water in a periodic box of size $24 \times 24 \times 9 \text{ nm}^3$ (the magnitude and units of $\langle |\tilde{h}(\mathbf{k})|^2 \rangle$ depend on the box size and Fourier transform convention). Electrostatic interactions were evaluated via the particle-mesh Ewald method and Lennard-Jones interactions were cut off at 1.2 nm. The spectrum at high wavevectors is sensitive to atomistic detail and to the coarse-graining length ξ used to define the intrinsic interface. Fitting the $\xi = 2.0 \text{ \AA}$ data in the range $0.01 \text{ \AA}^{-1} < k < 0.3 \text{ \AA}^{-1}$ yields $\gamma = 62.0 \pm 0.5 \text{ mJ/m}^2$, in reasonable agreement with the experimental value of 72 mJ/m^2 and some recent measurements of the SPC/E surface tension (e.g., $63.6 \pm 1.5 \text{ mJ/m}^2$ from Ref. [21]), but not others (e.g., 52.91 mJ/m^2 from Ref. [43]).

This results in N^2 discrete sampling points $\{\mathbf{a}\}$, with $N = D/\Delta$. In the following, sums over \mathbf{a} denote sums over these N^2 sampling points. We have used $D = 60 \text{ \AA}$ and $\Delta = 1 \text{ \AA}$.

The discrete variables $\{h_{\mathbf{a}}\}$ represent the interface height at each sample point \mathbf{a} , so that

$$h_{\mathbf{a}} = h(\mathbf{a}), \quad \text{for } \mathbf{a} = (n_x\Delta, n_y\Delta).$$

This notation clearly distinguishes between the N^2 height variables $h_{\mathbf{a}}$ and the continuous height function $h(\mathbf{a})$ that they represent.

The discrete Fourier transform of $\{h_{\mathbf{a}}\}$ is denoted by $\{\tilde{h}_{\mathbf{k}}\}$, and is defined at wavevectors $\mathbf{k} = (2\pi/L)(m_x, m_y)$, with $-N/2 \leq m_x, m_y < N/2$. We use the symmetric normalization convention throughout for Fourier transforms.

Energetics

The essential property of the liquid-vapor-like interface is its surface tension, which results in the following capillary-wave Hamiltonian [44] for a free interface,

$$H_0[\{h_{\mathbf{a}}\}] \approx \frac{\gamma\Delta^2}{2} \sum_{\mathbf{a}} |\nabla h_{\mathbf{a}}|^2 \approx \frac{\gamma\Delta^2}{2} \sum_{\mathbf{k}} k^2 |\tilde{h}_{\mathbf{k}}|^2,$$

where $\nabla h_{\mathbf{a}}$ is a finite-difference approximation to $\nabla h(\mathbf{a})$.

Using an appropriate definition of an instantaneous water-vapor interface [42], the power spectrum of capillary waves in SPC/E water has been found to agree with the spectrum predicted by the above Hamiltonian for wavevectors smaller than about $2\pi/\ell$, but is substantially lower for higher wavevectors (Fig. 6 of main text). This result is consistent with the liquid-vapor-like interfaces being sensitive to molecular detail at high wavevectors [43]. At $T = 300\text{ K}$, we have found that $\ell \approx 9\text{ \AA}$. We thus constrain all Fourier components $\tilde{h}_{\mathbf{k}}$ to be zero for high \mathbf{k} , i.e.

$$\tilde{h}_{\mathbf{k}} = 0, \quad |\mathbf{k}| > 2\pi/\ell. \quad (7)$$

In our model, the liquid-vapor-like interface interacts with a model surface via a potential that depends on $\{h_{\mathbf{a}}\}$. As discussed below, it is also convenient to introduce additional umbrella potentials to aid in sampling. The Hamiltonian of the interface subject to this additional potential energy $H'[\{h_{\mathbf{a}}\}]$ is

$$H[\{h_{\mathbf{a}}\}] = \frac{\gamma\Delta^2}{2} \sum_{\mathbf{k}} k^2 |\tilde{h}_{\mathbf{k}}|^2 + H'[\{h_{\mathbf{a}}\}]. \quad (8)$$

When expressed as a function of the Fourier components $\{\tilde{h}_{\mathbf{k}}\}$, we denote the Hamiltonian by $\tilde{H}[\{\tilde{h}_{\mathbf{k}}\}]$ and the external potential by $\tilde{H}'[\{\tilde{h}_{\mathbf{k}}\}]$, so that

$$\tilde{H}[\{\tilde{h}_{\mathbf{k}}\}] = \frac{\gamma\Delta^2}{2} \sum_{\mathbf{k}} k^2 |\tilde{h}_{\mathbf{k}}|^2 + \tilde{H}'[\{\tilde{h}_{\mathbf{k}}\}].$$

Dynamics

We calculate thermal averages of interface configurations by introducing a fictitious Langevin dynamics and replacing thermal averages by trajectory averages. We first assign a mass per unit area μ to the interface. The Lagrangian in real space is

$$L[\{h_{\mathbf{a}}, \dot{h}_{\mathbf{a}}\}] = \frac{\mu\Delta^2}{2} \sum_{\mathbf{a}} \dot{h}_{\mathbf{a}}^2 - H[\{h_{\mathbf{a}}\}].$$

The corresponding Lagrangian in Fourier space is

$$\tilde{L}[\{\tilde{h}_{\mathbf{k}}, \dot{\tilde{h}}_{\mathbf{k}}\}] = \frac{\mu\Delta^2}{2} \sum_{\mathbf{k}} |\dot{\tilde{h}}_{\mathbf{k}}|^2 - \tilde{H}[\{\tilde{h}_{\mathbf{k}}\}].$$

Since all $h_{\mathbf{a}}$ are real, the amplitudes of modes \mathbf{k} and $-\mathbf{k}$ are related, $\tilde{h}_{\mathbf{k}} = \tilde{h}_{-\mathbf{k}}^*$. Taking this constraint and Equation (7) into account, the Euler-Lagrange equations yield equations of motion in Fourier space. To thermostat each mode, we add Langevin damping and noise terms. The final equation of motion has the form

$$\mu\Delta^2\ddot{\tilde{h}}_{\mathbf{k}} = -\gamma\Delta^2|\mathbf{k}|^2\tilde{h}_{\mathbf{k}} - \frac{\partial\tilde{H}'[\{\tilde{h}_{\mathbf{k}}\}]}{\partial\tilde{h}_{\mathbf{k}}} - \eta\dot{\tilde{h}}_{\mathbf{k}} + \tilde{\xi}_{\mathbf{k}}(t), \quad (|\mathbf{k}| < 2\pi/\ell), \quad (9)$$

The Langevin damping constant η is chosen to decorrelate momenta over a timescale τ , so $\eta = \mu\Delta^2/\tau$. The zero-mean Gaussian noise terms $\{\tilde{\xi}_{\mathbf{k}}(t)\}$ have variance such that

$$\langle\tilde{\xi}_{\mathbf{k}}^*(t)\tilde{\xi}_{\mathbf{k}}(t')\rangle = 2\eta k_{\text{B}}T\delta(t-t').$$

As with $\tilde{h}_{\mathbf{k}}$, $\tilde{\xi}_{\mathbf{k}}$ satisfy the related constraint $\tilde{\xi}_{\mathbf{k}} = \tilde{\xi}_{-\mathbf{k}}^*$. Hence, for $\mathbf{k} = \mathbf{0}$, the noise is purely real and its variance is twice that of the real and imaginary components of all other modes [45].

We propagate these equations of motion using the Velocity Verlet algorithm. At each force evaluation, we use a Fast Fourier Transform (FFT) to calculate $\{h_{\mathbf{a}}\}$ from $\{\tilde{h}_{\mathbf{k}}\}$. We then calculate $\partial H'[\{h_{\mathbf{a}}\}]/\partial h_{\mathbf{a}}$ in real space and perform an inverse FFT to obtain the force $\partial\tilde{H}'[\{\tilde{h}_{\mathbf{k}}\}]/\partial\tilde{h}_{\mathbf{k}}$ on mode $\tilde{h}_{\mathbf{k}}$ due to $H'[\{h_{\mathbf{a}}\}]$. We then add the forces due to surface tension, Langevin damping and thermal noise, as in Eq. (9).

For the Velocity Verlet algorithm to be stable, we choose a timestep equal to $1/20^{\text{th}}$ of the typical timescale of the highest-frequency mode of the free interface, $\Delta t = \frac{1}{20}\sqrt{\mu\ell^2/\gamma}$. To equilibrate the system quickly but still permit natural oscillations, we choose the Langevin damping timescale so that $\tau = 100\Delta t$. Finally, we choose a value of μ close to the mass of a single water layer, $\mu = 100 \text{ amu/nm}^2$.

This interface dynamics is entirely fictitious. However, it correctly samples configurations of the interface Boltzmann-weighted by the Hamiltonian $H[\{h_{\mathbf{a}}\}]$. This is true irrespective of the exact values of μ , Δt and τ , so our choices have no effect on the results in the main text. We have simply chosen reasonable values that do not lead to large discretization errors when solving the system's equations of motion.

Surface-interface interactions

The liquid-vapor-like interface interacts with the model surface via a potential $H'_{\text{surf}}[\{h_{\mathbf{a}}\}]$. In the atomistic simulations, the SAM sets up an interaction potential $U(\mathbf{r})$ felt by the atoms in the water molecules. Below, we use the notation \mathbf{r} and (x, y, z) interchangeably. To model this interaction potential, we smear out the atomistic detail of the SAM and replace it with three elements:

- A uniform area density μ_{head} of Lennard-Jones sites (with length and energy scales σ_{head} and ϵ_{head}) in the $z = 0$ plane to represent the SAM head groups.
- A uniform volume density ρ_{tail} of Lennard-Jones sites (with length and energy scales σ_{tail} and ϵ_{tail}) in the half-space $z < -\zeta$ to represent the SAM tail groups.
- Coarse-graining the head-group atoms into a uniform area density results in a softer repulsive potential allowing the interface to penetrate far deeper into the model surface than would be possible in the actual SAM. To rectify this, we apply a strongly repulsive linear potential in the half-space $z < R_0$, where R_0 is the radius of the head group's hard core. The repulsive potential is chosen to be $1 k_{\text{B}}T$ when 1 nm^2 of interface penetrates the region $z < R_0$ by a "skin depth" δ .

The head groups are thus modeled by the following potential acting on a water molecule at position \mathbf{r} :

$$U_{\text{head}}(x, y, z \geq R_0) = \mu_{\text{head}} \int_{-\infty}^{\infty} dx' \int_{-\infty}^{\infty} dy' u_{\text{LJ}}(|\mathbf{r} - \mathbf{r}'|; \epsilon_{\text{head}}, \sigma_{\text{head}}) \Big|_{z'=0},$$

where $u_{\text{LJ}}(r; \epsilon, \sigma) = 4\epsilon[(\sigma/r)^{12} - (\sigma/r)^6]$ is the Lennard-Jones pair potential. Similarly, the effect of the tail groups is captured by

$$U_{\text{tail}}(x, y, z \geq R_0) = \rho_{\text{tail}} \int_{-\infty}^{\infty} dx' \int_{-\infty}^{\infty} dy' \int_{-\infty}^{-\zeta} dz' u_{\text{LJ}}(|\mathbf{r} - \mathbf{r}'|; \epsilon_{\text{tail}}, \sigma_{\text{tail}}).$$

Finally, the repulsive wall is modeled by the potential

$$U_{\text{wall}}(x, y, z < R_0) = 2\rho_{\ell}^{-1} \cdot (1 k_{\text{B}}T/1 \text{ nm}^2)(R_0 - z)/\delta,$$

where $\rho_{\ell} = 0.03333 \text{ \AA}^{-3}$ is the number density of liquid water.

These smeared interaction potentials depend only on z , not on x or y . As described in the main text, we also scale the head-group interaction by a parameter η . Putting everything together, we obtain an explicit expression for the surface-interface interaction potential,

$$H'_{\text{surf}}[\{h_{\mathbf{a}}\}] = \rho_{\ell} \Delta^2 \sum_{\mathbf{a}} h'_{\text{surf}}(h_{\mathbf{a}}),$$

where

$$h'_{\text{surf}}(h_{\mathbf{a}}) = \int_{h_{\mathbf{a}}}^{\infty} dz \eta U_{\text{head}}(z) + U_{\text{tail}}(z) + U_{\text{wall}}(z),$$

$$= \begin{cases} \eta \pi \epsilon_{\text{head}} \mu_{\text{head}} \sigma_{\text{head}}^3 \left[\frac{4}{45} (\sigma_{\text{head}}/z)^9 - \frac{2}{3} (\sigma_{\text{head}}/z)^3 \right] \\ \quad + \pi \epsilon_{\text{tail}} \rho_{\text{tail}} \sigma_{\text{tail}}^4 \left[\frac{1}{90} (\sigma_{\text{head}}/[z + \zeta])^8 - \frac{1}{3} (\sigma_{\text{head}}/[z + \zeta])^2 \right], & z \geq R_0, \\ h'_{\text{surf}}(R_0) + \rho_{\ell}^{-1} \cdot (1 \text{ k}_B T / 1 \text{ nm}^2) ([R_0 - z]/\delta)^2, & z < R_0. \end{cases}$$

To model the -CH₃ SAM in this paper, we chose the following values for the parameters

- The head groups are modeled as OPLS united-atom CH₃ groups interacting with SPC/E water, so $\sigma_{\text{head}} = 3.5355 \text{ \AA}$ and $\epsilon_{\text{tail}} = 0.68976 \text{ kJ/mol}$.
- The tail groups are modeled as OPLS united-atom CH₂ groups (sp³-hybridized) interacting with SPC/E water, so $\sigma_{\text{tail}} = 3.5355 \text{ \AA}$ and $\epsilon_{\text{tail}} = 0.5664 \text{ kJ/mol}$.
- The tail region is inset from the plane of the head groups by a distance equal to a CH₂-CH₃ bond length (1.50 Å), minus the van der Waals radius of a CH₂ group (1.9525 Å), so $\zeta = -0.4525 \text{ \AA}$.
- The head group density is known from the atomistic SAM geometry to be $\mu_{\text{head}} = 0.0462 \text{ \AA}^{-2}$. The mass density of the SAM tails was estimated to be 935 kg/m^3 [11], resulting in a CH₂ group number density of $\rho_{\text{tail}} = 0.0402 \text{ \AA}^{-3}$.
- The equivalent hard sphere radius R_0 of a -CH₃ group at room temperature was estimated to be 3.37 \AA [13]. It has a small temperature dependence, which we neglect.
- The wall skin depth δ was set to 0.1 \AA , which is small enough so that the repulsive potential is essentially a hard wall at $z = R_0$, but large enough that we can propagate the interfacial dynamics with a reasonable timestep.

Umbrella sampling

Calculating $\mu^{\text{ex}}(V)$ from Equation (2) of the main text as a thermal average $\langle P_v(0) \rangle$ over Boltzmann-weighted configurations of $h(\mathbf{a})$ is impractical for large V . The configurations that dominate this average simply have a vanishingly small Boltzmann weight. To solve this problem, and in analogy to what we do in atomistic simulations, we perform umbrella sampling on the size of the sub-volume v of the probe cavity V that is above the interface.

We begin by defining the volume V corresponding to a probe cavity of dimensions $L \times L \times W$ as the set of points satisfying $|x|, |y| \leq L/2$ and $R_0 \leq z \leq R_0 + W$. We then define $v[\{h_{\mathbf{a}}\}]$ as the size of the sub-volume of V that is above the interface. Using umbrella sampling and the multistate Bennet acceptance ratio method (MBAR) [46], we calculate the probability distribution for v , $P(v)$, down to $v = 0$. To do this, we use quadratic umbrellas defined by a center \bar{v} and width $(\delta v)^2$, which result in the addition to the Hamiltonian of

$$H'_{\text{umb}}[\{h_{\mathbf{a}}\}] = k_{\text{B}}T \frac{(v[\{h_{\mathbf{a}}\}] - \bar{v})^2}{2(\delta v)^2}.$$

During each umbrella run, we also record the configurations $\{h_{\mathbf{a}}\}$ which yield each observed value of v . We then approximate the right-hand side of Equation (2) in the main text by summing over these configurations with appropriate weights, and obtain

$$\mu^{\text{ex}}(V) \approx -k_{\text{B}}T \ln \frac{\sum_{\{h_{\mathbf{a}}\}} P_v(0) P(v[\{h_{\mathbf{a}}\}])}{\sum_{\{h_{\mathbf{a}}\}} P(v[\{h_{\mathbf{a}}\}])},$$

where, as in the main text, the term $P_v(0)$ depends on the interface configuration $\{h_{\mathbf{a}}\}$, and the sum $\{h_{\mathbf{a}}\}$ is over all interface configurations in all the different umbrellas. To evaluate $P_v(0)$, we implement discrete versions of the integrals defining $\langle N \rangle_v$ and σ_v as was done in Ref. [18].

-
- [1] K. Lum, D. Chandler, and J. D. Weeks, *J. Phys. Chem. B* **103**, 4570 (1999).
 - [2] D. Chandler, *Nature* **437**, 640 (2005).
 - [3] S. Rajamani, T. M. Truskett, and S. Garde, *P. Natl. Acad. Sci. U.S.A.* **102**, 9475 (2005).
 - [4] G. Hummer, S. Garde, A. E. Garcia, A. Pohorille, and L. R. Pratt, *P. Natl. Acad. Sci. U.S.A.* **93**, 8951 (1996).
 - [5] D. Chandler, *Phys. Rev. E* **48**, 2898 (1993).

- [6] L. R. Pratt and D. Chandler, *J. Chem. Phys.* **67**, 3683 (1977).
- [7] S. Garde, G. Hummer, A. E. Garcia, M. E. Paulaitis, and L. R. Pratt, *Phys. Rev. Lett.* **77**, 4966 (1996).
- [8] F. H. Stillinger, *J. Solution Chem.* **2**, 141 (1973).
- [9] D. M. Huang and D. Chandler, *P. Natl. Acad. Sci. U.S.A.* **97** (2000).
- [10] B. J. Berne, J. D. Weeks, and R. Zhou, *Ann. Rev. Phys. Chem.* **60**, 85 (2009).
- [11] R. Godawat, S. N. Jamadagni, and S. Garde, *P. Natl. Acad. Sci. U.S.A.* **106**, 15119 (2009).
- [12] N. Shenogina, R. Godawat, P. Keblinski, and S. Garde, *Phys. Rev. Lett.* **102**, 156101 (2009).
- [13] A. J. Patel, P. Varilly, and D. Chandler, *J. Phys. Chem. B* **114**, 1632 (2010).
- [14] A. J. Patel, P. Varilly, D. Chandler, and S. Garde, *J. Stat. Phys.*, submitted (2011).
- [15] H. J. C. Berendsen, J. R. Grigera, and T. P. Straatsma, *J. Phys. Chem.* **91**, 6269 (1987).
- [16] B. Widom, *J. Chem. Phys.* **39**, 2808 (1963).
- [17] G. E. Crooks and D. Chandler, *Phys. Rev. E* **56**, 4217 (1997).
- [18] P. Varilly, A. J. Patel, and D. Chandler, *J. Chem. Phys.* **134**, 074109 (2011).
- [19] A. H. Narten and H. A. Levy, *J. Chem. Phys.* **55**, 2263 (1971).
- [20] W. L. Jorgensen, J. D. Madura, and C. J. Swenson, *J. Am. Chem. Soc.* **106**, 6638 (1984).
- [21] C. Vega and E. de Miguel, *J. Chem. Phys.* **126**, 154707 (2007).
- [22] D. M. Huang, P. L. Geissler, and D. Chandler, *J. Phys. Chem. B* **105**, 6704 (2001).
- [23] J. Alejandre, D. J. Tildesley, and G. A. Chapela, *J. Chem. Phys.* **102**, 4574 (1995).
- [24] M. V. Athawale, S. Sarupria, and S. Garde, *J. Phys. Chem. B* **112**, 5661 (2008).
- [25] L. Maibaum, A. R. Dinner, and D. Chandler, *J. Phys. Chem. B* **108**, 6778 (2004).
- [26] W. Kauzmann, *Adv. Prot. Chem.* **14**, 1 (1959).
- [27] P. R. ten Wolde and D. Chandler, *P. Natl. Acad. Sci. U.S.A.* **99**, 6539 (2002).
- [28] T. F. Miller, E. Vanden-Eijnden, and D. Chandler, *P. Natl. Acad. Sci. U.S.A.* **104**, 14559 (2007).
- [29] X. Huang, R. Zhou, and B. J. Berne, *J. Phys. Chem. B* **109**, 3546 (2005).
- [30] C. J. Beverung, C. J. Radke, and H. W. Blanch, *Biophys. Chem.* **81**, 59 (1999).
- [31] A. Sethuraman, G. Vedantham, T. Imoto, T. Przybycien, and G. Belfort, *Proteins* **56**, 669 (2004).
- [32] A. Nikolic, S. Baud, S. Rauscher, and R. Pomes, *Proteins* **79**, 1 (2011).
- [33] S. N. Jamadagni, R. Godawat, J. S. Dordick, and S. Garde, *J. Phys. Chem. B* **113**, 4093

- (2009).
- [34] W. Fenton and A. Horwich, *Q. Rev. Biophys.* **36**, 229 (2003).
 - [35] J. England, D. Lucent, and V. Pande, *Curr. Opin. Struc. Biol.* **18**, 163 (2008).
 - [36] A. Jewett and J.-E. Shea, *Cell. Mol. Life Sci.* **67**, 255 (2010).
 - [37] G. Makhatadze and P. Privalov, *Adv. Prot. Chem.* **47**, 307 (1995).
 - [38] S. S. Karajanagi, A. A. Vertegel, R. S. Kane, and J. S. Dordick, *Langmuir* **20**, 11594 (2004).
 - [39] H. Acharya, S. Vembanur, S. N. Jamadagni, and S. Garde, *Faraday Discuss.* **146**, 353 (2010).
 - [40] N. Giovambattista, P. G. Debenedetti, and P. J. Rossky, *J. Phys. Chem. C* **111**, 1323 (2007).
 - [41] J. Mittal and G. Hummer, *Faraday Discuss.* **146**, 341 (2010).
 - [42] A. P. Willard and D. Chandler, *J. Phys. Chem. B* **114**, 1954 (2010).
 - [43] F. Sedlmeier, D. Horinek, and R. R. Netz, *Phys. Rev. Lett.* **103**, 136102 (2009).
 - [44] F. Buff, R. Lovett, and F. H. Stillinger, *Phys. Rev. Lett.* **15**, 621 (1965).
 - [45] The constraint on the magnitude of \mathbf{k} ensures that no Nyquist modes, i.e., modes with k_x or k_y equal to $\pm\pi/D$, are ever excited. If they were included, these modes would also be purely real, and the variance of the real component of their noise terms would likewise be twice that of the real component of the interior modes.
 - [46] M. R. Shirts and J. D. Chodera, *J. Chem. Phys.* **129**, 124105 (2008).